Journal of the Association of Arab Universities for Basic and Applied Sciences (2016) **21**, 38–44

University of Bahrain

Journal of the Association of Arab Universities for Basic and Applied Sciences

www.elsevier.com/locate/jaaubas
www.sciencedirect.com

ORIGINAL ARTICLE

Characterization and antibacterial activity of nanocrystalline Mn doped Fe_2O_3 thin films grown by successive ionic layer adsorption and reaction method

M.R. Belkhedkar [a,b], A.U. Ubale [a,*], Y.S. Sakhare [a], Naushad Zubair [c], M. Musaddique [c]

[a] *Nanostructured Thin Film Materials Laboratory, Department of Physics, Govt. Vidarbha Institute of Science and Humanities, VMV Road, Amravati 444604, Maharashtra, India*
[b] *Department of Physics, Shri Shivaji College, Akola 444003, Maharashtra, India*
[c] *Department of Microbiology, Shri Shivaji College, Akola 444003, Maharashtra, India*

Received 25 November 2014; revised 24 February 2015; accepted 11 March 2015
Available online 8 June 2015

KEYWORDS

Thin film;
Nanostructures;
Biomaterials;
Optical properties;
Antibacterial activity

Abstract Successive ionic layer adsorption and reaction (SILAR) method have been successfully employed to grow nanocrystalline Mn doped α-Fe_2O_3 thin films onto glass substrates. The structural analysis revealed that, the films are nanocrystalline in nature with rhombohedral structure. The optical studies showed that α-Fe_2O_3 thin film exhibits 3.02 eV band gap energy and it decreases to 2.95 eV as the Mn doping percentage in it was increased from 0 to 8 wt.%. The SILAR grown α-Fe_2O_3 film exhibits antibacterial character against *Staphylococcus aureus* bacteria and it increases remarkably with Mn doping.

1. Introduction

Since the past decades, α-Fe_2O_3 has gained extensive scientific importance in materials science because of its important role in various applications namely gas sensor, supercapacitor, dye sensitized solar cell, photocatalyst, lithium ion battery and in microbial fuel cells (Lee et al., 2001; Fan et al., 2011; Mulenko et al., 2012; Rahman and Joo, 2013; Cavas et al., 2013; Akhavan, 2010; Hsien et al., 2013; Kitaura et al., 2008; Kulal et al., 2011; Ji et al., 2011). In recent years, many researchers have studied the role of doping in α-Fe_2O_3 to improve its applicability for electrochemical sensors, solid oxide fuel cell and photo splitting of water etc. (Suresh et al., 2012; Geng et al., 2012; Shwarsctein et al., 2008). In addition, Shinde et al. (2011) have reported structural, morphological, luminescent and electronic properties of spray deposited Al doped α-Fe_2O_3 thin films. Khan and Zhou (1993) have reported physical properties of iodine doped α-Fe_2O_3 thin films grown by spray pyrolysis. Sanchez et al. (1988) have

* Corresponding author. Tel.: +91 721 2531706; fax: +91 721 2531705.
E-mail address: ashokuu@yahoo.com (A.U. Ubale).
Peer review under responsibility of University of Bahrain.

http://dx.doi.org/10.1016/j.jaubas.2015.03.001
1815-3852

reported photoelectrochemical properties of niobium doped α-Fe_2O_3 thin films grown by chemical vapor deposition method. Sensing properties of LPD synthesized Pd and Ca doped α-Fe_2O_3 thin films were reported by Neri et al. (2007). As per literature to grow doped and undoped α-Fe_2O_3 thin films, various chemical deposition methods have been utilized viz. spin coating deposition (Souza et al., 2009), liquid-phase method (Neri et al., 2001), electrodeposition (Kumar et al., 2011), spray-pyrolysis (Kumari et al., 2010) and DC sputtering (Kiran et al., 2006). The growth of nanostructured thin films by a simple and economic deposition technique has been playing an important role in the field of nanoscience and nanotechnology in order to reduce the device fabrication cost. In this paper, we have outlined the simple and economic successive ionic layer adsorption and reaction method to grow nanocrystalline Mn doped α-Fe_2O_3 thin films. This is an excellent method to grow a nanocrystalline thin film by immersing the glass substrate into separately placed cationic and anionic precursors alternately. In between each immersion, the substrate is rinsed in deionized water to remove the loosely bound species to get an adherent thin film. As cationic and anionic precursors are separately placed, it is very easy to control the growth process by adjusting the number of deposition cycles. The structural, morphological and optical properties of nanocrystalline Mn doped α-Fe_2O_3 thin films grown by the SILAR method are discussed in the paper. Also, the results of antibacterial activity of the Mn doped α-Fe_2O_3 films against *Staphylococcus aureus* bacteria are reported.

2. Experimental

2.1. Preparation of Mn doped α-Fe_2O_3 thin films

To grow Mn doped α-Fe_2O_3 thin films 0.3 M $MnCl_2$ of pH 1 and 0.06 M $FeCl_2$ of pH <1 were used as cationic precursors along with 0.005 M NaOH (pH ≈ 12) solution as an anionic precursor. The beakers containing precursor solutions were placed alternately in such a way that, every cationic and anionic precursor was followed by a beaker containing deionized water. Several deposition trials were performed to optimize the various deposition parameters to grow Mn_3O_4 and α-Fe_2O_3 films separately. For α-Fe_2O_3 film, a well cleaned glass substrate was immersed in a cationic precursor for 20 s where Fe^{3+} ions were adsorbed on the substrate surface. The substrate was then rinsed in deionized water for 20 s to remove loosely bound Fe^{3+} ions. Finally it was immersed in NaOH solution for 20 s, where OH^- ions react with Fe^{3+} ions to form α-Fe_2O_3 species. This was again followed by rinsing in deionized water for 20 s to remove loose material from the substrate surface. This completes one SILAR deposition cycle for α-Fe_2O_3. The immersion and rinsing time periods were experimentally optimized to get uniform and adherent thin films. The optimized deposition parameters for Mn_3O_4 films were already explained in our earlier report (Ubale et al., 2012). To achieve proper doping, several deposition trials were performed by varying the concentration of Fe precursor to match the growth rate of α-Fe_2O_3 film formation with Mn_3O_4. It was observed that, the growth rate of α-Fe_2O_3 and Mn_3O_4 is approximately the same for 0.06 and 0.3 M concentrations of $FeCl_3$ and $MnCl_2$ respectively. Fig. 1 shows the variation of Mn_3O_4 and α-Fe_2O_3 film thickness with a number of deposition cycles. It was observed

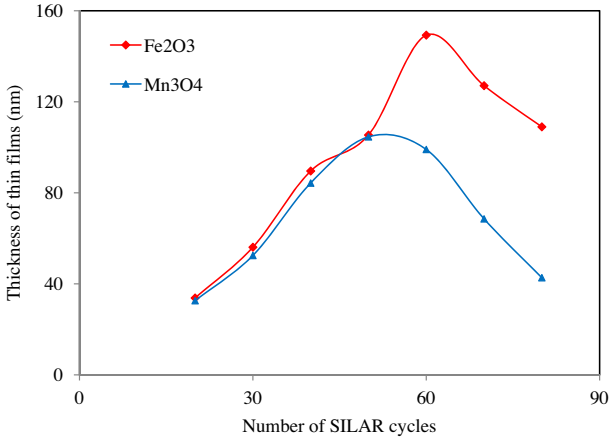

Figure 1 Plot of α-Fe_2O_3 and Mn_3O_4 film thickness with number of SILAR cycles [Cationic Source: 0.06 M $FeCl_3$ (for Fe_2O_3) and 0.3 M $MnCl_2$ (for Mn_3O_4)].

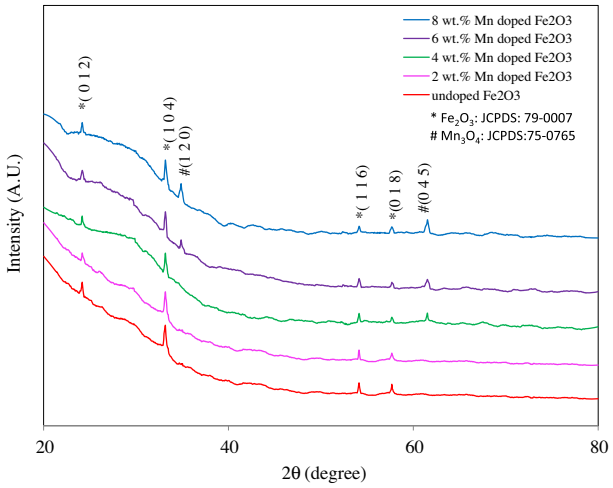

Figure 2 GIXRD patterns of Mn doped α-Fe_2O_3 thin films.

Table 1 Film thickness and crystallite size of α-Fe_2O_3 with Mn doping percentage.

wt.% of Mn in α-Fe_2O_3	Film thickness (nm)	Average crystallite size from	
		GIXRD (nm)	FESEM (nm)
0	105	21	28
2	108	21	26
4	107	20	23
6	105	19	21
8	106	17	20

that up to 50 SILAR cycles the growth rate was approximately the same. Above 50 SILAR cycles, thickness of Mn_3O_4 film decreases as it peels off; however, the thickness of α-Fe_2O_3 film increases up to 60 SILAR cycles. Hence for the present work, to grow Mn doped α-Fe_2O_3 thin films 50 SILAR cycles were considered. To achieve 0, 2, 4, 6 and 8 wt.% doping of Mn in α-Fe_2O_3, the number of SILAR cycles for (Fe_2O_3:Mn_3O_4) composition were taken as (50:0), (49:1), (48:2), (47:3) and (46:4) respectively. These films were further annealed at 500° C for

3 h to get a pure metal oxide phase of the deposited material and used for further characterization.

2.2. Characterization techniques

In the present work, thickness of the film was measured by gravimetric weight difference method by using the relation,

$$t = \frac{m}{\rho \times \mathrm{A}} \quad (1)$$

where 'm' is the mass of the deposited material measured by using a sensitive microbalance; 'A' is the area of the deposited film in cm^2 and 'ρ' is the density of the deposited material. It was observed that, the thickness of Mn doped α-Fe_2O_3 thin films deposited by repeating 50 SILAR cycles is of the order of 105 nm. The crystal structure of the deposited film was identified by grazing incidence X-ray diffraction with Xpert PRO PANalytical diffractometer. The surface morphological investigations were carried out by using field emission scanning electron microscope (Model: SUPRA 40) and atomic force microscope (Model: Nanonics Multiview 2000™, Israel). The optical absorption studies were carried out in the wavelength range 350–750 nm using ELICO® Double Beam SL 210 UV–Vis spectrophotometer.

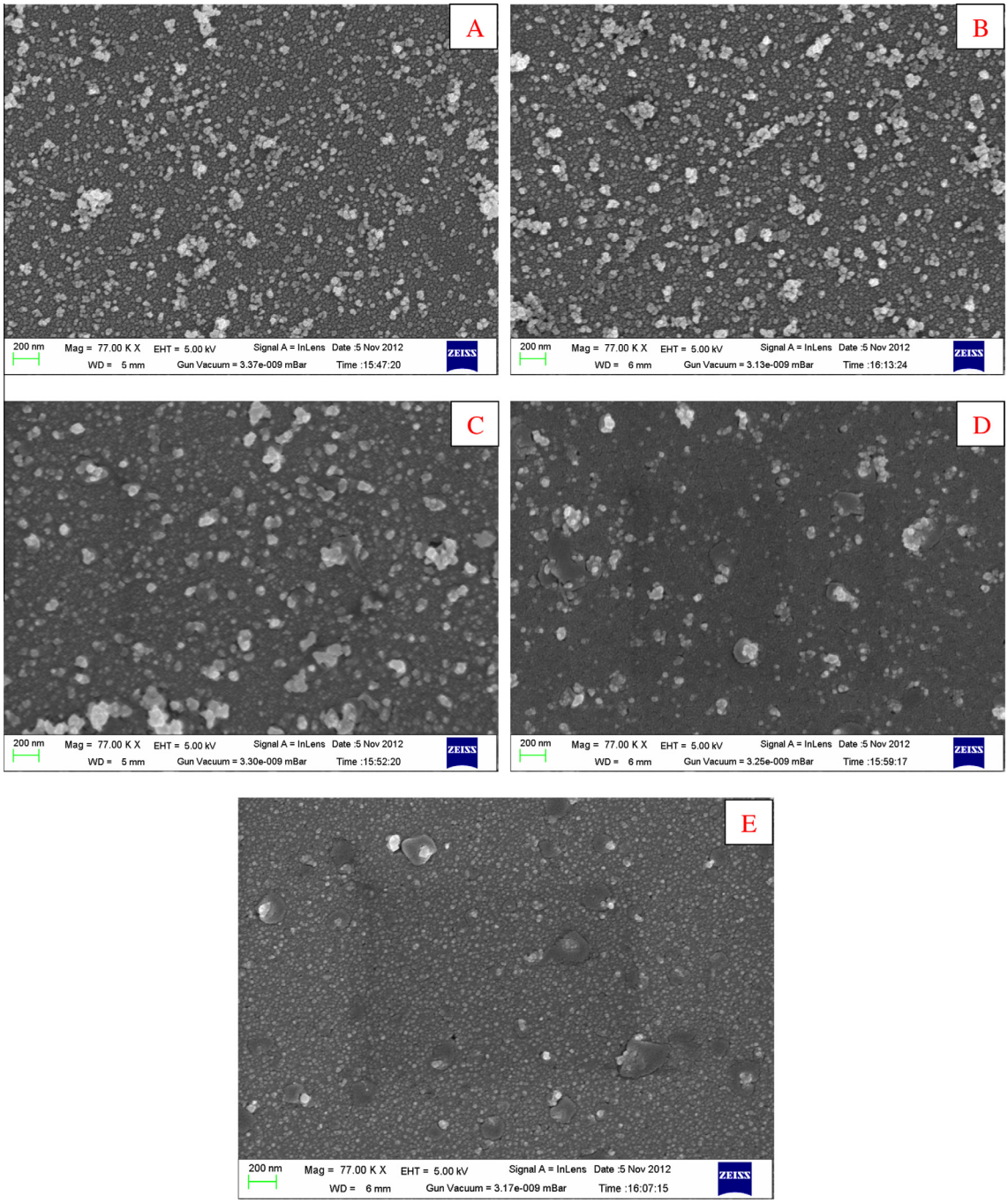

Figure 3 FESEM images of Mn doped α-Fe_2O_3 thin films; Mn doping percentage: (A) 0 wt.%, (B) 2 wt.%, (C) 4 wt.%, (D) 6 wt.% and (E) 8 wt.%.

2.3. Antibacterial test

A spread plate technique was employed to investigate antibacterial behavior of Mn doped α-Fe_2O_3 thin films against *S. aureus*. For it, the culture of *S. aureus* bacteria was prepared in nutrient broth. The loopful culture of *S. aureus* organisms was further inoculated into 20 mL sterilized nutrient broth and incubated at 310 K for 24 h. Then, 20 μL cultures of *S. aureus* was inoculated on undoped and Mn doped iron oxide glass substrates of area 1 cm^2 with the help of an inoculating needle. These glass slides were then placed in previously sterilized petri dishes and incubated at 310 K for 24 h. After incubation these slides were transferred to 3 mL of buffer peptone solution in a test tube and ultrasonicated to detach the bacteria thoroughly from the substrate. From this, 20 μL washed buffer peptone solution was then inoculated on nutrient agar plates by a spread plate technique and incubated at 310 K for 24 h to obtain viable bacteria. After successful incubation the viable bacterial colonies were counted and antibacterial efficiency was calculated using the relation (Zhang et al., 2008),

$$r = \frac{(N_0 - N)}{N_0} \times 100\% \quad (2)$$

where, 'r' is the antibacterial efficiency, 'N_0' is the number of viable bacterial colonies observed in the petri dish from undeposited film and 'N' is the number of viable bacterial colonies observed in the petri dish from Mn doped Fe_2O_3 thin film.

3. Results and discussion

3.1. Structural studies

Fig. 2 shows typical GIXRD patterns of Mn doped iron oxide thin films. The pattern revealed that SILAR grown Fe_2O_3 films are nanocrystalline in nature with rhombohedral structure. The observed GIXRD data are in good agreement with the standard data [JCPDS: 79-0007 and JCPDS: 75-0765]. The (0 1 2), (1 0 4), (1 1 6) and (0 1 8) orientations observed in the patterns are due to α-Fe_2O_3, which is in good agreement with the results reported by several workers (Akhavan, 2010; An et al., 2009; Cha et al., 2009). For higher wt.% of Mn doping (0 4 5) and (1 2 0) peaks due to Mn_3O_4 are observed. It is also observed that the intensity of diffraction peaks due to Mn_3O_4 increases with doping percentage. The average crystallite size of the deposited material was determined by using Debye–Scherer formula (Ubale et al., 2013),

$$D = \frac{0.9\lambda}{\beta \mathrm{Cos}\theta} \quad (3)$$

where 'λ' is the wavelength used (0.154 nm); 'β' is the angular line width at half maximum intensity in radians and 'θ' is the Bragg's angle. It is found that the crystallite size of the α-Fe_2O_3 film is of the order of 21 nm, and it decreases to 17 nm as doping percentage of Mn was increased from 0 to 8 wt.% (Table 1).

3.2. Surface morphology

The surface morphology of the iron oxide thin films deposited onto glass substrates by the SILAR method was examined by using field emission scanning electron micrographs (Fig. 3). The FESEM analysis shows compact and homogeneous distribution of nano grains of varying sizes from 28 to 20 nm depending upon doping percentage. The agglomeration of nano grains is observed at several places on the film surface. It is seen that the number of agglomerated grains reduces with Mn doping. The grain sizes estimated from FESEM images are in good agreement with GIXRD results (Table 1).

The elemental analysis of the undoped and 6 wt.% Mn doped α-Fe_2O_3 thin films were carried out using energy dispersive X-ray (EDX) analysis (Fig. 4). The elemental analysis was carried only for Fe, O and Mn elements. The additional peaks observed in the spectra are due to the composition of the glass substrate. The small minor peak of Mn observed in the spectra confirms its doping in α-Fe_2O_3.

Fig. 5 shows 3D AFM images of Mn doped α-Fe_2O_3 thin films. The images were recorded in tapping mode by using an optical fiber tip, coated with gold and chromium (Au, Cr) metal with φ = 20 nm at response frequency 52.38 kHz. The AFM analysis showed that the granular structure of α-Fe_2O_3 is uniformly distributed over the entire substrate surface. The morphological parameters such as rms roughness (Rq), average roughness (Ra), average height, maximum height and grain orientation depending on doping percentage of Mn are listed in Table 2. The rms roughness of α-Fe_2O_3 film decreases as doping concentration of Mn rises from 0 to 8 wt.%. The rms roughness and average roughness becomes approximately equal above 6 wt.% doping of Mn which may be because of uniform mixing of Mn_3O_4 in α-Fe_2O_3.

3.3. Optical studies

The optical absorption measurements for α-Fe_2O_3 thin films deposited onto glass substrates were carried out in the wavelength

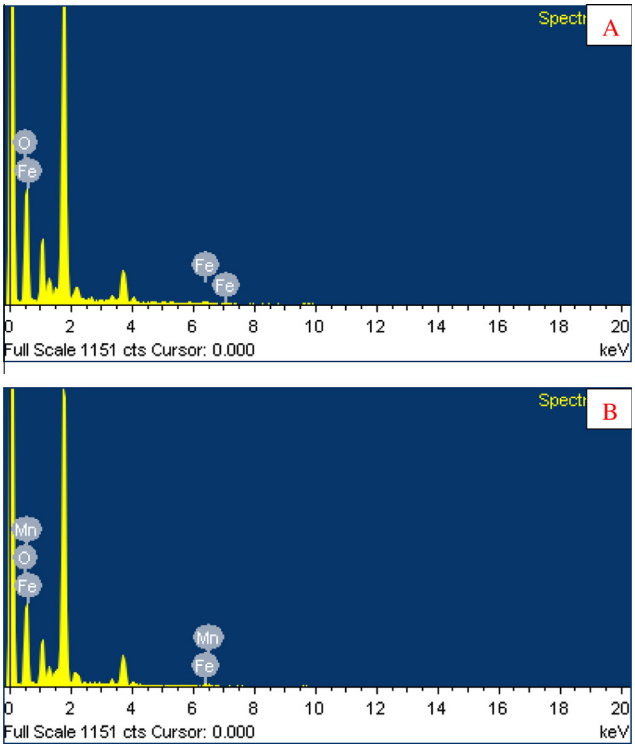

Figure 4 EDAX spectrum (A) as deposited Fe_2O_3 film and (B) 6 wt.% Mn doped α-Fe_2O_3 film.

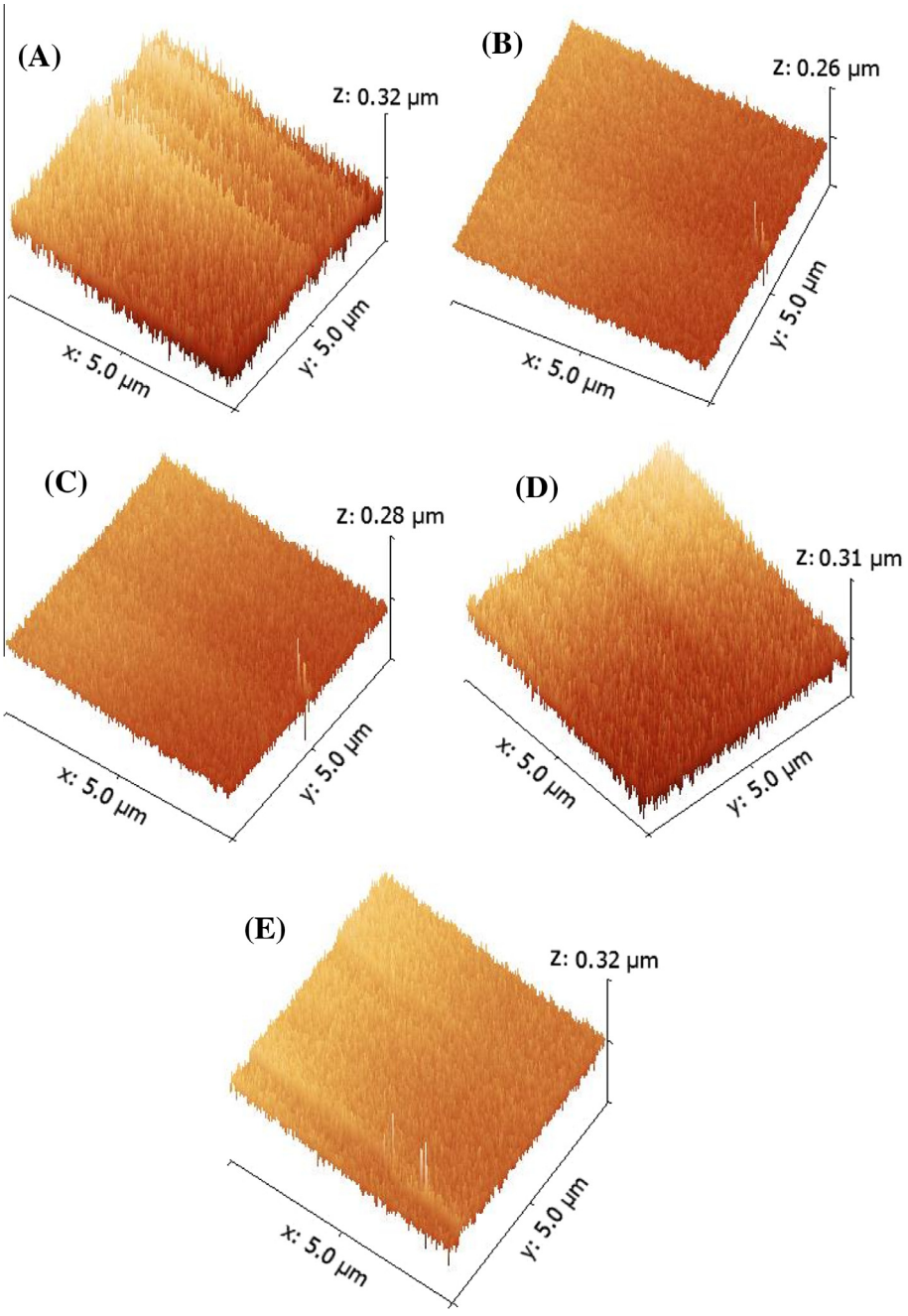

Figure 5 3D AFM images of Mn doped α-Fe_2O_3 thin films; Mn doping percentage: (A) 0 wt.%, (B) 2 wt.%, (C) 4 wt.%, (D) 6 wt.% and (E) 8 wt.%.

Table 2 Morphological parameters of Mn doped α-Fe_2O_3 thin films.

wt.% of Mn in Fe_2O_3	RMS roughness Rq (nm)	Average surface roughness Ra(nm)	Maximum height (nm)	Average height (nm)	Grain orientation (pi)
0	86.01	71.83	323.2	121.72	0.07
2	77.53	62.14	267.5	118.01	0.16
4	71.05	59.82	280.6	117.34	0.08
6	68.72	57.45	317.4	114.3	0.08
8	66.15	54.03	326.6	112.78	0.12

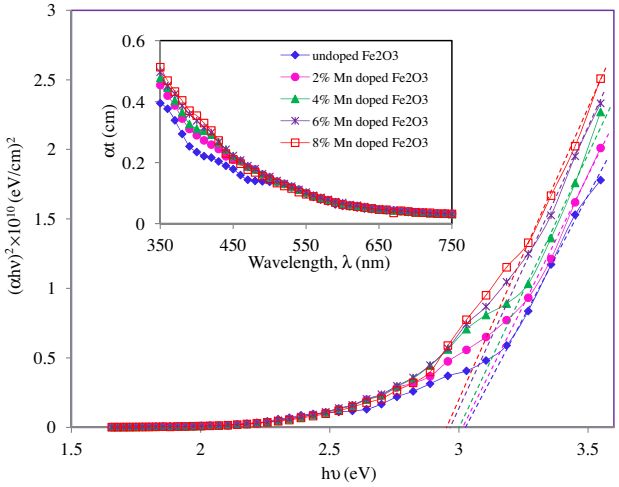

Figure 6 The plots of $(\alpha h\nu)^2$ versus $h\nu$ (Inset plots of optical absorption versus wavelength) of Mn doped α-Fe_2O_3 thin films.

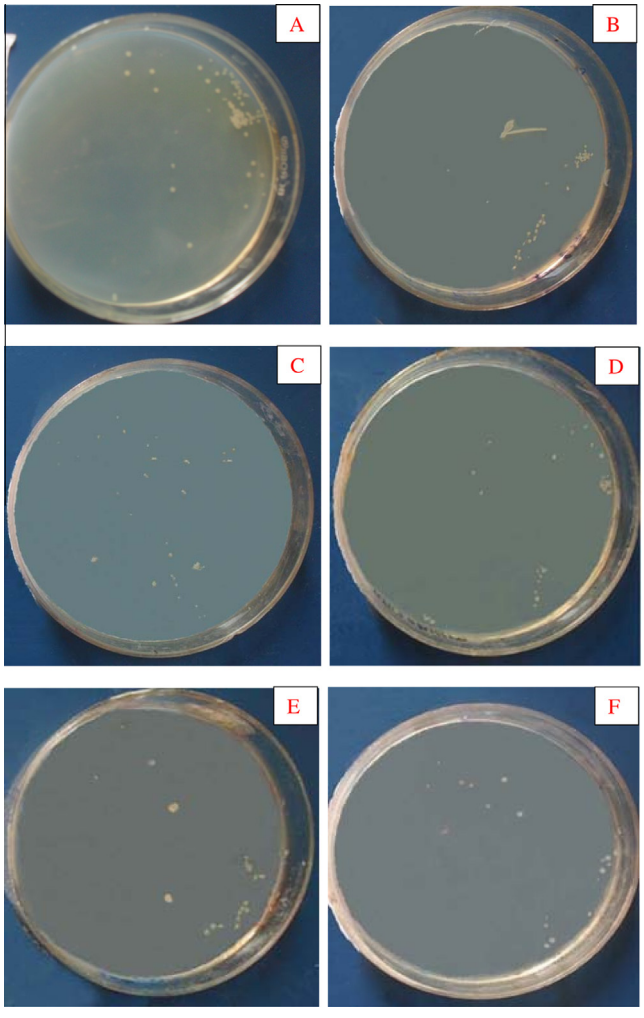

Figure 7 Antibacterial test results of *S. aureus* after 24 h: incubated on (A) undeposited glass substrate and on Mn doped α-Fe_2O_3 thin films with Mn doping (B) 0 wt.%, (C) 2 wt.%, (D) 4 wt.%, (E) 6 wt.% and (F) 8 wt.%.

range 350–750 nm at room temperature shown in the inset of Fig. 6. An increase in the optical absorption of α-Fe_2O_3 films was observed with increase in doping percentage of Mn. The optical band gap energies (Eg) of undoped and Mn doped α-Fe_2O_3 films were calculated by using the equation (Mahdi et al., 2012),

$$\alpha h\upsilon = A(h\upsilon - Eg)^n \quad (4)$$

where, 'α' is absorption coefficient, 'Eg' is band gap energy, 'A' is a constant and 'n' is equal to 1/2 for direct and 2 for indirect transition. Fig. 6 illustrates the plots of $(\alpha h\nu)^2$ versus $h\nu$ for Mn doped α-Fe_2O_3 thin films. The band gap energy 'Eg' of the α-Fe_2O_3 film was estimated by extrapolating the linear portion of the plot to the energy axis and is found to be of the order of 3.02 eV. This estimated optical band gap energy of the α-Fe_2O_3 thin film is in good agreement with the results reported by Glasscock et al. (2008) and Bhar et al. (2010). However, it is observed that, the optical band gap energy of the film decreases from 3.02 to 2.95 eV as Mn doping in α-Fe_2O_3 rises from 0 to 8 wt.%.

3.4. Antibacterial activity

The antibacterial character of the Mn doped α-Fe_2O_3 thin films were investigated against *S. aureus* bacteria. The test results of *S. aureus* bacteria incubated at 24 h on undeposited glass substrate and Mn doped α-Fe_2O_3 thin film surfaces are shown in Fig. 7. It was observed that, the antibacterial efficiency for undoped α-Fe_2O_3 film is 16.66% and it increases to 58.33% as doping of Mn increases from 0 to 8 wt.%. This increased antibacterial efficiency may be due to the improved nanocrystalline nature of α-Fe_2O_3 films. But, the interactions of nanoparticles with bacteria are dependent on the size, shape and morphology of the deposited material (Yu et al., 2011; Sikong et al., 2010). When these nanoparticles come in contact with a bacterial cell, an active oxygen is formed due to the chemisorption process, as a result more number of iron, manganese and hydroxide ions or hydrogen peroxide were released from the surface, which can react with the peptide linkages in the cell wall of bacteria and disrupt them. This antibacterial mechanism may be involved in the antibacterial study to kill the *S. aureus* microorganisms (Zhang et al., 2008; Touati, 2000; Keenan and Sedlak, 2008; Ubale and Belkhedkar, 2015; Belkhedkar and Ubale, 2014; Aninwene et al., 2013). It was also observed from the AFM images that the rms roughness of α-Fe_2O_3 film decreases with the increase of Mn doping, which plays a very important role in the antibacterial activity against the *S. aureus* bacteria. Due to decreased rms roughness of the film, more nanoparticles of deposited material interacted with the bacteria and damaged the cell wall which further blocks the bacterial production. As the rms roughness of the α-Fe_2O_3 thin films is almost closure above 4 wt.% doping of Mn, its antibacterial activity against *S. aureus* bacteria becomes nearly constant. Similarly, the role of rms roughness on the antibacterial activity of nano-barium sulfate incorporated pellethane bio-film against *S. aureus* and *Pseudomonas aeruginosa* bacteria was reported by Aninwene et al. (2013).

4. Conclusions

In the present work, Mn doped α-Fe_2O_3 thin films were successfully synthesized by successive ionic layer adsorption and reaction method onto glass substrates. The GIXRD,

FESEM, EDX and AFM characterizations confirm that as grown Mn doped α-Fe_2O_3 thin films are nanocrystalline in nature. The optical band gap energy of α-Fe_2O_3 thin film increases with the doping percentage of Mn. The optical band gap energy and film morphology can be engineered by adjusting the doping of Mn in α-Fe_2O_3, so as to make them suitable for optoelectronic devices. Also, the antibacterial character of α-Fe_2O_3 against *S. aureus* bacteria enhances remarkably with Mn doping.

References

Akhavan, O., 2010. Thickness dependent activity of nanostructured TiO_2/α-Fe_2O_3 photocatalyst thin films. Appl. Surf. Sci. 257, 1724–1728.

An, Z.G., Zhang, J.J., Pan, S.L., 2009. Facile preparation and characterization of glass/α-Fe_2O_3 core/shell composite hollow spheres with the shell layer assembled by disk-like petals. Mater. Chem. Phys. 117, 209–213.

Aninwene II, G.E., Stout, D., Yang, Z., Webster, T.J., 2013. Nano-$BaSO_4$: a novel antimicrobial additive to pellethane. Int. J. Nanomed. 8, 1197–1205.

Belkhedkar, M.R., Ubale, A.U., 2014. Physical properties of nanostructured Mn_3O_4 thin films synthesized by SILAR method at room temperature for antibacterial application. J. Mol. Struct. 1068, 94–100.

Bhar, S.K., Mukherjee, N., Maji, S.K., Adhikary, B., Mondal, A., 2010. Synthesis of nanocrystalline iron oxide ultrathin films by thermal decomposition of iron nitroprusside: structural and optical properties. Mater. Res. Bull. 45, 1948–1953.

Cavas, M., Gupta, R.K., Al-Ghamdi, A.A., Gafer, Z.H., Tantawy, F.E., Yakuphanoglu, F., 2013. Preparation and characterization of dye sensitized solar cell based on nanostructured Fe_2O_3. Mater. Lett. 105, 106–109.

Cha, H.G., Kim, C.W., Kim, Y.H., Jim, M.H., Ji, E.S., Das, B.K., Kim, J.C., Kang, Y.S., 2009. Preparation and characterization of α-Fe_2O_3 nanorod-thin film by metal–organic chemical vapor deposition. Thin Solid Films 517, 1853–1856.

Fan, H., Zhang, T., Xu, X., Lv, N., 2011. Fabrication of N-type Fe_2O_3 and P-type $LaFeO_3$ nanobelts by electrospinning and determination of gas-sensing properties. Sens. Actuators B 153, 83–88.

Geng, S., Qi, S., Zhao, Q., Zhu, S., Wang, F., 2012. Electroplated Ni doped Fe_2O_3 composite coating for solid oxide fuel cell interconnect application. Int. J. Hydrogen Energy 37, 10850–10856.

Glasscock, J.A., Barnes, P.R.F., Plumb, I.C., Bendavid, A., Martin, P.J., 2008. Structural, optical and electrical properties of undoped polycrystalline hematite thin films produced using filtered arc deposition. Thin Solid Films 516, 1716–1724.

Hsien, W.Y., Dong, Z.L., Li, C.F., Yen, S.K., 2013. Characterization of electrolytic deposited α-Fe_2O_3 thin films on stainless steel as anodes for Li-ion batteries. Surf. Coat. Technol. 216, 52–59.

Ji, J., Jia, Y., Wu, W., Bai, L., Ge, L., Gu, Z., 2011. A layer-by-layer self-assembled Fe_2O_3 nanorod based composite multilayer film on ITO anode in microbial fuel cell. Colloids Surf. A: Physicochem. Eng. Aspects 390, 56–61.

Keenan, C.R., Sedlak, D.L., 2008. Factors affecting the yield of oxidants from the reaction of nanoparticulate zero valent iron and oxygen. Environ. Technol. 42 (4), 1262–1267.

Khan, S.U.M., Zhou, Z.Y., 1993. Photoresponse of undoped and iodine-doped iron oxide thin film electrodes. J. Elecrtoanal. Chem. 357, 407–420.

Kiran, M.S.R.N., Sudheendran, K., Krishna, M.G., James, R.K.C., Bhatnagar, A.K., 2006. Chromium and nickel substituted iron oxide thin films by DC sputtering. Vacuum 81, 133–137.

Kitaura, H., Takahashi, K., Mizuno, F., Hayashi, A., Tadanaga, K., Tatsumisago, M., 2008. Mechanochemical synthesis of α-Fe_2O_3 nanoparticles and their application to all-solid-state lithium batteries. J. Power Sources 183, 418–421.

Kulal, P.M., Dubal, D.P., Lokhande, C.D., Fulari, V.J., 2011. Chemical synthesis of Fe_2O_3 thin films for supercapacitor application. J. Alloy Compd. 509, 2567–2571.

Kumar, P., Sharma, P., Shrivastav, R., Dass, S., Satsangi, V.R., 2011. Electrodeposited zirconium-doped α-Fe_2O_3 thin film for photoelectrochemical water splitting. Int. J. Hydrogen Energy 36, 2777–2784.

Kumari, S., Singh, A.P., Sonal, Deva D., Shrivastav, R., Dass, S., Satsangi, V.R., 2010. Spray pyrolytically deposited nanoporous Ti^{4+} doped hematite thin films for efficient photoelectrochemical splitting of water. Int. J. Hydrogen Energy 35, 3985–3990.

Lee, E.T., Jang, G.E., Kim, C.K., Yoon, D.H., 2001. Fabrication and gas sensing properties of α-Fe_2O_3 thin film prepared by plasma enhanced chemical vapor deposition (PECVD). Sens. Actuators B 77, 221–227.

Mahdi, M.A., Hassan, J.J., Hassan, Z., Ng, S.S., 2012. Growth and characterization of $Zn_xCd_{1-x}S$ nanoflowers by microwave-assisted chemical bath deposition. J. Alloys Compd. 541, 227–233.

Mulenko, S.A., Petrov, Y.N., Gorbachuk, N.T., 2012. Photon synthesis of iron oxide thin films for thermo-photo-chemical sensors. Appl. Surf. Sci. 258, 9186–9191.

Neri, G., Bonavita, A., Galvagno, S., Pace, C., Patane, S., Arena, A., 2001. Humidity sensing properties of Li-iron oxide based thin films. Sens. Actuators B 73, 89–94.

Neri, G., Bonavita, A., Ipsale, S., Rizzo, G., Baratto, C., Faglia, G., Sberveglieri, G., 2007. Pd- and Ca-doped iron oxide for ethanol vapor sensing. Mater. Sci. Eng. B 139, 41–47.

Rahman, G., Joo, O.S., 2013. Electrodeposited nanostructured α-Fe_2O_3 thin films for solar water splitting: influence of Pt doping on photoelectrochemical performance. Mater. Chem. Phys. 140, 316–322.

Sanchez, C., Sieber, K.D., Somorjai, G.A., 1988. The photoelectrochemistry of niobium doped α-Fe_2O_3. J. Electroanal. Chem. 252, 269–290.

Shinde, S.S., Moholkar, A.V., Kim, J.H., Rajpure, K.Y., 2011. Structural, morphological, luminescent and electronic properties of sprayed aluminium incorporated iron oxide thin films. Surf. Coat. Technol. 205, 3567–3577.

Shwarsctein, A.K., Hu, Y., Forman, A.J., Stucky, J.D., McFarland, E., 2008. Electrodeposition of α-Fe_2O_3 doped with Mo or Cr as photoanodes for photocatalytic water splitting. J. Phys. Chem. C 112, 15900–15907.

Sikong, L., Kongreong, B., Kantachote, D., Sutthisripok, W., 2010. Photocatalytic activity and antibacterial behavior of Fe^{3+} doped TiO_2/SnO_2 nanoparticles. Energy Res. J. 1 (2), 120–125.

Souza, F.L., Lopes, K.P., Nascente, P.P., Leite, E.R., 2009. Nanostructured hematite thin films produced by spin-coating deposition solution: application in water splitting. Sol. Energy Mater. Sol. Cells 93, 362–368.

Suresh, R., Rrabu, R., Vijayaraj, A., Giribabu, K., Stephen, A., Narayanan, V., 2012. Facile synthesis of cobalt doped hematite nanospheres: magnetic and their electrochemical sensing properties. Mater. Chem. Phys. 134, 590–596.

Touati, D., 2000. Iron and oxidative stress in bacteria. Arch. Biochem. Biophys. 373 (1), 1–6.

Ubale, A.U., Belkhedkar, M.R., Sakhare, Y.S., Singh, A., Gurada, C., Kothari, D.C., 2012. Characterization of nanostructured Mn_3O_4 thin films grown by SILAR method at room temperature. Mater. Chem. Phys. 136, 1067–1072.

Ubale, A.U., Sakhare, Y.S., Bhute, M.V., Belkhedkar, M.R., Singh, A., 2013. Size dependent structural, electrical and optical properties of nanostructured iron selenide thin films deposited by chemical bath deposition method. Solid State Sci. 16, 134–142.

Ubale, A.U., Belkhedkar, M.R., 2015. Size dependent physical properties of nanostructured α-Fe_2O_3 thin films grown by successive ionic layer adsorption and reaction method for antibacterial application. J. Mater. Sci. Technol. 31 (1), 1–9.

Yu, B., Leung, K.M., Guo, Q., Lau, W.M., Yang, J., 2011. Synthesis of Ag-TiO2 composite nano thin film for antimicrobial application. Nanotechnology 22, 115603–115611.

Zhang, W., Chen, Y., Yu, S., Chen, S., Yin, Y., 2008. Preparation and antibacterial behavior of Fe^{3+}-doped nanostructured TiO_2 thin films. Thin Solid Films 516, 4690–4694.